Cohesive/adhesive strengths of CsOH-chemisorbed SS304 surfaces

Nabaichuan Li[a], Yifan Sun[a], Kunihisa Nakajima[b], and Ken Kurosaki[a,c]

[a]Institute for Integrated Radiation and Nuclear Science, Kyoto University, Kumatori, Osaka 590-0494, Japan; [b]Nuclear Science and Engineering Center, Japan Atomic Energy Agency, Tokai-mura, Naka-gun, Ibaraki 319-1195, Japan; [c]Research Institute of Nuclear Engineering, University of Fukui, Tsuruga, Fukui 914-0055, Japan

ABSTRACT
During the Fukushima Daiichi Nuclear Power Plant (1F) accident, volatile radioactive fission products (FPs) such as Cs-137 were released, which significantly influenced mid- to long-term decommissioning strategies. A substantial amount of the remaining cesium in the pressure vessel may have deposited onto the 304 stainless steel (SS304) steam separators and dryers. This deposited cesium presents a safety hazard during 1F's decommissioning, as it can generate radioactive dust and complicate waste storage. However, the cohesive and adhesive strengths of CsOH-chemisorbed oxide scales, crucial for understanding the release of cesium-bearing particles from SS304 surfaces, remain undefined. In this study, we explore how CsOH chemisorption affects the cohesive and adhesive strengths between oxide scales and SS304 substrates using a scratch tester. Our tests revealed that cracks formed at approximately the same load, but the overall cohesive strength of the oxide scales decreased following CsOH chemisorption. Furthermore, the transition from cracks to bulk separation occurred more rapidly in CsOH-chemisorbed SS304 substrates, especially those with lower silicon content. Finally, we found that adhesive failure could not be achieved even at 70 N, suggesting that the deposited cesium cannot be completely removed from SS304 during the decommissioning of 1F.

1. Introduction

On March 11, 2011, a magnitude 9.0 earthquake hit the Fukushima Daiichi Nuclear Power Plant (1F), and a subsequent tsunami led to a complete blackout at 1F. With the loss of cooling functions, Units 1-3 experienced varying levels of loss-of-coolant accidents (LOCA), and core meltdowns occurred[1,2]. During these meltdowns, nearly 100% of the volatile fission products (FPs), such as cesium and iodine, were released from the fuel rods[3–6]. Among these FPs, Cs-137 has a high yield and a half-life of 30 years, significantly impacting the medium and long-term decommissioning strategies for 1F[7].

The transport and distribution of cesium shortly after the meltdown have been extensively investigated using severe accident (SA) codes[3–6,8–10]. A mid-to-long-

---

Corresponding author. Email: sun.yifan.7r@kyoto-u.ac.jp

Corresponding author. Email: kurosaki.ken.6n@kyoto-u.ac.jp

term analysis was provided by Uchida et al[11]. By 2014, Shibata et al.[12] estimated that approximately 50% of the initial cesium inventory remained in the reactor. High radiation dose rates were detected near the drywell head and shield plug areas[13, 14], which are primarily attributed to the reaction between CsOH and $CaCO_3$[15]. Despite these findings, Okumura et al.[16] suggested that dose rates within the reactor pressure vessel (RPV) might exceed those within the containment. Furthermore, recent OECD/NEA benchmark studies highlight that the RPV could contain a significantly larger amount of cesium than the containment and reactor building due to in-vessel cesium deposition[5,6,8].

Under SA conditions, the primary cesium species present are CsOH and CsI[17], which can condense onto the surfaces of the 304-grade stainless steel (SS304) within the RPV. SS304 typically oxidizes slightly when exposed to high-temperature steam, forming a duplex oxide scale on its surface[18–20]. While CsI vapor only condenses onto SS304 below 1270 K[21,22], CsOH vapor can diffuse into oxidized SS304, and the amount of retained cesium positively correlates with the silicon content in the SS304 substrate[18,19,23–27]. The cesium retention ability of SS304 has also been shown to depend on the presence of pre-existing oxide layers before the chemisorption process[28]. Furthermore, factors such as solutes (e.g. Mo in SS316 and Ti in SS321), temperature, CsOH concentration, and the H_2/H_2O ratio in the atmosphere are known to affect the kinetics and products of CsOH chemisorption[19,26,27,29–31].

During SAs, the SS304 steam separators and steam dryers located at the top head of the RPV can capture a significant amount of the transported CsOH due to their extended surface areas and complex structures. These structures may become the primary sources of cesium-bearing dust during decommissioning. Similar to alpha radioactive nuclei, the release of cesium-bearing particles must be controlled to minimize the risk of radiation exposure[32]. Achieving this goal requires a comprehensive understanding of the properties, generation, and transport of cesium dust.

While previous studies have clarified the reactions between CsOH and SS304, the mechanism by which the oxide layer containing CsOH detaches from SS304 surfaces remains unclear. In this study, we use the scratch testing technique to investigate the impact of CsOH chemisorption conditions on the cohesive strength of the oxide scale and the interfacial adhesive strength between the oxide layer and SS304 substrate. We also identify the failure modes that occur as the applied load increases, using optical microscopy. This scratch-test study is part of our ongoing investigation of the effects of CsOH chemisorption on SS304, and structural analyses on CsOH-chemisorbed SS304 oxide scale have been previously reported[25]. Together, these results will contribute to a better understanding of the release of airborne cesium-bearing dust due to mechanical interactions with SS304 surfaces during the decommissioning of the Fukushima Daiichi Nuclear Power Plant.

2. Experiment method

2.1. Sample preparation and characterization

The CsOH chemisorption tests were conducted using the setup illustrated in Figure 1. In a nickel crucible, 0.5 g of CsOH·H_2O (Kanto Chemicals, purity $\geq$ 85%) was first heated to 1173 K and held at that temperature for 30 minutes to prevent abrupt evaporation. Following this, CsOH·H_2O was fully vaporized at 1273 K over a period of three hours. SS304 samples with a silicon content of either 0.2 or 1.0 wt.% were

heated to 1073 or 1273 K, mirroring the conditions inside the RPV dome during SA at 1F[33,34]. The samples were held at these temperatures for 4.0 hours (at 1073 K) and 3.5 hours (at 1273 K), respectively. After chemisorption, the samples were slowly cooled at an approximate rate of 10 K/min. Two graphs showing the recorded temperatures of different components during the experiments are provided in Figures S1 and S2 in the supporting information. The compositions of the SS304 substrates are listed in Table 1, and their diffraction patterns are presented in Figure S3 in the supporting information.

[Figure 1 about here.]

[Table 1 about here.]

During the chemisorption process, both $Ar/5\%H_2$ and $Ar/5\%H_2/5\%H_2O$ gas mixtures were flowed at a rate of 200 mL/min. Seven CsOH-chemisorbed SS304 samples were prepared under various conditions (silicon content, temperature, and gas flow), which are listed in Table 2. Samples 6 and 12 were used as controls and were not exposed to CsOH vapor. As it is likely that air ingress occurred in the furnace during heating[25], this study does not delve into the effect of the atmosphere on the cohesive/adhesive properties in great detail. For more information on sample preparation and the CsOH deposition process, refer to our earlier work[25].

[Table 2 about here.]

The surfaces of CsOH-chemisorbed SS304 samples underwent analysis using X-ray diffraction (XRD, Rigaku SmartLab) and scanning electron microscopy-energy dispersive spectroscopy (SEM–EDS, JEOL JSM-7610F). XRD measurements were performed within the range of $2\theta = 20 - 120°$ using $CuK\alpha$ radiation. To determine the thickness and structure of the oxide scales on the SS304 substrates, cross-sections of the chemisorbed samples were examined using SEM–EDS.

2.2. Scratch test

The scratch test is a measurement technique utilized to evaluate the cohesive and adhesive strengths of coatings and thin films[35–39]. It's crucial to note that this test provides only a semi-quantitative assessment of a coating's cohesive and adhesive strengths. This is because the critical loads (L_c) associated with various cohesive and adhesive failure modes depend on factors related to both the indenter and the coating/substrate[36–38,40]. In the context of this study, cohesive strength refers to the internal bond strength of the coating, while adhesive strength measures the bond strength at the coating/substrate interface.

In this study, we used the Revetest Scratch Tester (S/N: 27-486, CSM Instruments), a simplified schematic of which is shown in Figure 2. The diamond indenter, with a tip diameter of 200 μm, scratched the top surfaces of the samples (Figure 1) from right to left at a constant speed of 10 mm/min. The initial load was 0.9 N, which increased at a rate of 100 N/min, and the scratch tester stopped when the load reached 70 N. Each sample was subjected to three scratch tests at temperatures between 297–299 K and a humidity of 24–29%. A complete list of the scratch test conditions used in this study is presented in Table 3.

[Figure 2 about here.]

[Table 3 about here.]

Figure 3 illustrates the various pieces of information recorded during the scratch test. The horizontal axis represents the horizontal displacement of the indenter, while the applied load is depicted by the black line. The friction force is shown in magenta, and the red line indicates the calculated coefficient of friction. The blue line corresponds to the recorded acoustic emission, which is associated with stress waves produced by active defects, such as crack propagation within the sample[37,41]. Lastly, the indentation depth is represented by the orange dashed line.

[Figure 3 about here.]

3. Results and discussion

3.1. Surface conditions

3.1.1. Non-chemisorbed samples 6 and 12

Figure 4 displays the XRD patterns of non-chemisorbed samples, specifically samples 6 and 12, both of which were heated to 1273 K in $Ar/H_2/H_2O$. The primary diffraction peaks in the XRD pattern can be attributed to a cubic Fe-Cr phase[42], which corresponds to the unoxidized SS304 substrate, and spinel iron oxides[43], the main components of the oxide scale[18,19,44]. The diffraction peaks indicated in Figure 4 are associated with trigonal phases such as Fe_2O_3 or Cr_2O_3. However, the indexed trigonal peaks are shifted compared to those of Fe_2O_3[45] and Cr_2O_3[46], suggesting the formation of $(Fe,Cr)_2O_3$ solid solutions. Due to the complexity of the oxide scale's structure, not every diffraction peak could be indexed.

[Figure 4 about here.]

Figure 5 presents the SEM-EDS results of non-chemisorbed sample 12. The surface EDS point analyses results for samples 6 and 12 are provided in Figure S4 in the supporting information, with the main difference being the absence of Si-concentrated regions in sample 6. As shown in Figure 5, the surface of sample 12 consists of three distinct regions, labeled 1, 2, and 3:

- Region 1, rich in Fe and Si, features a smoother surface with needle-shaped microstructures.
- Region 2, rich in Cr and Fe, is composed of small particles.
- Region 3 consists of chunks of Fe-Cr oxide, with the atomic ratio between Fe and Cr closely resembling that of the SS304 substrate ($\approx$ 3:1).

In the Fe-Si rich region 1, the amount of Si exhibits a positive correlation with the concentration of Fe and O, suggesting the presence of Fe-Si-O compounds. Although the formation of Fe_2SiO_4 within the oxide scale has been reported previously[44,47], its diffraction peaks were not detected during XRD, possibly due to the low concentration of silicon in the SS304 substrates. Furthermore, the Cr concentration detected by EDS significantly varies in region 1, which is likely due to overlaps between regions 1 and 2 (Fe-Cr oxides), as depicted in Figure 5. This overlap may also result in EDS point analyses overestimating the atomic ratio between Fe and Si in region 1 (Fe:Si$\approx$5). Lastly, clusters of Fe-Ni rich nodules can be seen along the boundaries between regions 1 and 2.

4

[Figure 5 about here.]

3.1.2. CsOH-chemisorbed samples

Figures 6 and 7 display the XRD patterns of chemisorbed samples. Phases not detected in non-chemisorbed samples (e.g., Cs-related peaks) are labeled above their corresponding diffraction peaks. The diffraction peaks of three types of Cs-containing species—$CsFeSiO_4$[48], $Cs_2Si_2O_5$[49], and $Cs_2Fe_2Si_4O_{12}$[50]—are detected. Samples 1, 8, and 11 likely contain a wustite phase (FeO)[51]. Although Cs was detected in sample 2 by SEM-EDS, the Cs-related diffraction peaks could not be identified due to their low intensity.

[Figure 6 about here.]

[Figure 7 about here.]

Since the intensity of the Cs-related diffraction peak is highest for sample 8, its SEM-EDS results are displayed in Figure 8 to clarify the distribution of Cs in the SS304 oxide scale after chemisorption. Additional information on the EDS results for samples 8, 9, and 11 is provided in Figure S5. For these three CsOH-chemisorbed SS304 substrates, EDS point analyses reveal a positive correlation between the concentrations of silicon and cesium, with the average atomic ratios between Si and Cs being approximately 1.0, 3.2, and 1.5, respectively. Overall, the atomic ratios are in agreement with the Cs-containing phases determined by XRD, taking into account that Si compounds without Cs could also form.

As depicted in Figures 8 and S5, the surface of CsOH-chemisorbed oxide scale generally consists of slightly oxidized Fe-Ni-Cr alloys, Fe-Cr oxides, and Cs-Si compounds. The Fe alloys appear as nodules, similar to the morphology found on the oxide scale of non-chemisorbed substrates in Figure 5. One exception is in sample 11 (1.0 wt.% Si, 1273 K, $Ar/H_2/H_2O$), where chunks of almost pure iron oxides were observed on top of the Fe-Cr oxides instead of Fe-Cr-Ni nodules. Furthermore, for all CsOH-chemisorbed SS304 surfaces, EDS point analyses reveal that the newly-formed Cs-Si compounds are always selectively deposited on Fe-Cr oxides.

[Figure 8 about here.]

3.2. Cross-section analyses

In CsOH-chemisorbed samples, the thickness of the oxide layer ranged from approximately 20 to 30 μm, showing no correlation with the chemisorption temperature or the silicon concentration of the substrate. The cross-sectional EDS point analysis result for sample 8 is shown in Figure 9, with additional EDS maps provided in Figure S6 in the supporting information.

[Figure 9 about here.]

The oxide scale of CsOH-chemisorbed SS304 substrate with low silicon content, heated between 1073 and 1273 K, can be divided into three layers. The majority of the Cs-Si compounds are concentrated near the top layer of the oxide scale, with few Cs-Si nodules present near the substrate/oxide interface. The intermediate layer, which constitutes the majority of the oxide scale, is composed of Fe-Cr oxides and Fe-Ni-Cr alloys. The Fe-Cr oxides, rich in Fe, are identified as $(Fe,Cr)_3O_4$ based on XRD data.

5

Additionally, the concentrations of Fe and Ni in the Fe-Ni-Cr regions exceed those of the SS304 substrate. The innermost layer of the oxide scale comprises Fe-Cr oxides with a higher concentration of Cr than that in the intermediate layer.

Despite the surface morphology of sample 11 differing from those of other CsOH-chemisorbed samples, its cross-section also exhibits a layered structure, as shown in Figure S7. However, the distinctions between the intermediate and inner layers of the oxide scale are less pronounced, with both containing Fe-Cr spinels and Fe-Ni-Cr alloys. The composition of the Fe-Ni-Cr alloys is similar to that found in sample 8, and Cr-rich spinels are also located close to the SS304/oxide interface. For further analyses on the surface and cross-sectional morphology of CsOH-chemisorbed SS304 substrates, please refer to our previous publications[23,25].

3.3. Scratch test results

Following the scratch tests, cohesive and adhesive failures were first determined by observing the surfaces of the SS304 substrates using an optical microscope. The results of the scratch tests for CsOH-chemisorbed and non-chemisorbed samples, specifically samples 11 and 12, are provided in Figures 10 and 11. Surface cracking was observed in both samples at relatively low indentation loads, and patches of glossy regions were seen at higher loads. Although these surface features were observed in all samples, it cannot be confirmed through optical microscopy alone whether the glossy regions resulted from the oxide scale's adhesive failure. The onset of adhesive failure is often indicated by an abrupt change in the coefficient of friction because the indenter is no longer pressed against the coating. However, no distinct changes in the recorded coefficients of friction were observed when the glossy regions first appeared. This leads to the conclusion that the glossy regions are not pristine SS, but rather are covered with thin oxide films after the bulk of the oxide scale has been removed during scratching.

[Figure 10 about here.]

[Figure 11 about here.]

The scratch test results revealed that the oxide scale experienced internal cohesive failure, but the adhesive bonding at the oxide/SS interface did not fail, even at the maximum applied load of 70 N. This suggests that it may not be possible to completely separate the oxide scale (with or without cesium species) from the SS304 steam separators and dryers. Furthermore, the high adhesive strength of the oxide scale means that if its bulk is removed through repetitive scratching underwater, the remaining layer will be tightly bonded to the SS304 substrate, resulting in fewer airborne Cs-bearing particles.

To better understand how the cohesive failure modes change with applied load, further investigation is needed. This is important because the amount of cesium released is correlated with the type of cohesive failure (cracks, chips, spalls). Therefore, we defined three distinct cohesive failure modes based on the morphology of the sample's surface, as listed in Table 4. By examining these failure modes, we hope to gain insights into the mechanisms that drive the cohesive failure of the oxide scale and improve our understanding of how cesium-bearing dust is generated.

[Table 4 about here.]

The critical load, L_c, and its standard deviation for each failure mode are presented

in Table 5 and Figure S8 (supporting information). It is noteworthy that the generation of Cs-bearing dust from surface cracks can occur as low as approximately 10 N, which has implications for 1F's decommissioning. Since adhesion failure was not observed during scratch testing, a constant release of Cs particles is expected with increasing load. Furthermore, sample 1 with 0.2 wt.% Si, chemisorbed at 1073 K under an Ar/H_2 mixed atmosphere, exhibits the weakest cohesive strength among all CsOH-chemisorbed samples.

[Table 5 about here.]

For all CsOH-chemisorbed samples, the coefficients of friction between the indenter and the oxide scale remain relatively constant, approximately between 0.1 and 0.3 (Table S1, supporting information), as the applied load increases from L_{c1} to L_{c3}. Although the critical loads for cracking (L_{c1}) showed little variation across the nine samples, the critical loads L_{c2} and L_{c3} related to bulk removal exhibited significant variation. Detailed comparisons of the individual effects of CsOH-chemisorption, temperature, and silicon content on the cohesive strength of the oxide scale are shown in Figures 12–14.

Effects of CsOH-chemisorption

Figure 12 illustrates that CsOH chemisorption marginally increases the critical load for cracking, L_{c1}, thereby enhancing the resistance of the Cs-bearing oxide scale to cracking. However, it significantly reduces the L_{c2} and L_{c3} of the oxide scale, which facilitates the removal of the bulk of the oxide scale. For instance, when SS304 substrates with 0.2 wt.% Si were heated to 1273 K in an $Ar/H_2/H_2O$ gas mixture, the critical load (L_{c3}) required to continuously remove the bulk of the oxide scale decreased from 31.3 to 19.7 N following CsOH chemisorption. This reduction in L_{c2} and L_{c3} leads to a decrease in the difference between L_{c1} and L_{c2}/ L_{c3}, suggesting that transitions among the three cohesive failure modes occur more rapidly. Therefore, precise control over the applied load when making contact with CsOH-chemisorbed SS304 surfaces is crucial to prevent accidental bulk removal and minimize dust generation.

[Figure 12 about here.]

Effects of temperature & silicon content

Although the compositions of the outgoing gas were not monitored, the critical load data in Figure 13 suggest that the correlation between chemisorption temperature and the cohesive strengths of the oxide scale (L_{c2}, L_{c3}) is dependent on the chemisorption atmosphere. This phenomenon is thought to be related to the differing revaporation behaviors of the insoluble cesium species under various atmospheres, as reported by Nishioka et al.[27]. Furthermore, the silicon concentration in the SS304 substrate is positively correlated with the critical loads L_{c2} and L_{c3}. As shown in Figure 14, L_{c2} and L_{c3} are found to be more influenced by the silicon content of the SS304 substrate when heated to lower temperatures, irrespective of the atmosphere.

[Figure 13 about here.]

[Figure 14 about here.]

4. Conclusion

A significant amount of the remaining cesium in 1F's reactors is expected to have deposited onto the SS304 surfaces of the steam separators and dryers in the RPV. In this study, the cohesive and adhesive strengths of the oxide scales were evaluated to gain insights into the dispersion of Cs-bearing dust during 1F's decommissioning. Across all nine SS304 samples, including CsOH-chemisorbed and non-chemisorbed samples, the critical load for cohesive surface cracking (L_{c1}) showed minimal variation and ranged from 10 to 20 N. At higher loads, the cohesive failure mode shifted to bulk removal, resulting in a significantly larger amount of Cs-bearing dust generation. CsOH-chemisorption reduced the critical loads for bulk removal (L_{c2} and L_{c3}), accelerating the transition between these cohesive failure modes. Therefore, it is crucial to carefully monitor mechanical contact with CsOH-chemisorbed SS304 surfaces to prevent the release of Cs-bearing particles. Adhesion failure was not observed during scratch testing, indicating continuous dust generation after reaching the critical load for cohesive failure. However, the thin oxide film remaining after removing the bulk of the oxide scale firmly adheres to the SS304 substrate, effectively inhibiting the release of Cs-bearing dust into the air.

Furthermore, the overall cohesive strength of the CsOH-chemisorbed oxide scale was found to be positively correlated with the silicon concentration of the SS304 substrate between 1073 and 1273 K. The correlation between chemisorption temperature and cohesive strength is influenced by the chemisorption atmosphere. Higher temperatures lead to stronger cohesive strength under Ar/H_2, while the addition of water vapor has the opposite effect. Combining these findings with simulation results on the core's condition during SA enables estimation of the RPV regions most likely to generate radioactive Cs-bearing dust through mechanical contact during 1F's decommissioning.

Data availability statement

The datasets generated and/or analyzed during this study are available from the corresponding authors upon reasonable request.

Disclosure statement

The authors have no competing interests to declare.

Funding

References

[1] Fukushima Nuclear Accident Analysis Report. Tokyo (Japan): Tokyo Electric Power Company, Inc.; 2012.
[2] Fukushima Daiichi: ANS Committee Report. Illinois (IL): American Nuclear Society; 2012.

[3] Gauntt R, Kalinich D, Cardoni J, et al. MELCOR simulations of the severe accident at the Fukushima Daiichi Unit 1 reactor. Nucl Technol. 2014;186(2):161–178.

[4] Fernandez-Moguel L, Rydl A, Lind T. Updated analysis of Fukushima Unit 3 with MELCOR 2.1. Part 2: Fission product release and transport analysis. Ann Nucl Energy. 2019; 130:93–106.

[5] Lind T, Pellegrini M, Herranz LE, et al. Overview and outcomes of the OECD/NEA benchmark study of the accident at the Fukushima Daiichi NPS (BSAF), Phase 2–Results of severe accident analyses for Unit 3. Nucl Eng Des. 2021;376. 111138.

[6] Herranz LE, Pellegrini M, Lind T, et al. Overview and outcomes of the OECD/NEA benchmark study of the accident at the Fukushima Daiichi NPS (BSAF) Phase 2–Results of severe accident analyses for Unit 1. Nucl Eng Des. 2020;369. 110849.

[7] Bowsher BR. Fission-product chemistry and aerosol behaviour in the primary circuit of a pressurized water reactor under severe accident conditions. Prog Nucl Energy. 1987; 20(3):199–233.

[8] Sonnenkalb M, Pellegrini M, Herranz LE, et al. Overview and outcomes of the OECD/NEA benchmark study of the accident at the Fukushima Daiichi NPS (BSAF), Phase 2–Results of severe accident analyses for Unit 2. Nucl Eng Des. 2020;369. 110840.

[9] Sevón T. A MELCOR model of Fukushima Daiichi Unit 1 accident. Ann Nucl Energy. 2015;85:1–11.

[10] Sevón T. A MELCOR model of Fukushima Daiichi Unit 3 accident. Nucl Eng Des. 2015; 284:80–90.

[11] Uchida S, Karasawa H, Kino C, et al. An approach toward evaluation of long-term fission product distributions in the Fukushima Daiichi nuclear power plant after the severe accident. Nucl Eng Des. 2021;380. 111256.

[12] Shibata A, Koma Y, Ohi T. Estimation of the inventory of the radioactive wastes in Fukushima Daiichi NPS with a radionuclide transport model in the contaminated water. J Nucl Sci Technol. 2016;53(12):1933–1942.

[13] Andrews N, Cardoni JN, Gauntt RO. Preliminary Assessment of the Dose near the Shield Plug at Fukushima Daiichi Unit 2 (1F2). Albuquerque (NM): Sandia National Lab; 2016. (SAND2016-5859C).

[14] Kawamura S, Ooki S, Narabayashi T. Measures to improve robustness of primary containment vessel and operation of filtered containment venting system based on the lessons from the containment leak at Fukushima Dai-ichi Nuclear Power Station Unit 2. Nippon Genshiryoku Gakkai Wabun Ronbunshi. 2016;15(2):53–65.

[15] Luu VN, Nakajima K. Study on cesium compound formation by chemical interaction of CsOH and concrete at elevated temperatures. J Nucl Sci Technol. 2023;60(2):153–164.

[16] Okumura K, Riyana ES, Wakaei S, et al. A method for the prediction of the dose rate distribution in a primary containment vessel of the Fukushima Daiichi Nuclear Power Station. Prog Nucl Sci Technol. 2019;6:108–112.

[17] Technical bases for estimating fission product behavior during LWR accidents. Washington (DC): U.S. Nuclear Regulatory Commission; 1981. (NUREG-0772).

[18] Elrick RM, Sallach RA, Ouellette AL, et al. Reaction between some cesium-iodine compounds and the reactor materials 304 stainless steel, Inconel 600 and silver. Volume 1: Cesium hydroxide reactions. Albuquerque (NM) and Livermore (CA): Sandia National Labs; 1984. (NUREG/CR-3197-Vol.1; SAND-83-0395-Vol.1).

[19] Bowsher BR, Dickinson S, Nichols AL. High temperature studies of simulant fission products. Pt. 3. Temperature-dependent interaction of caesium hydroxide vapour with 304 stainless steel. Winfrith (UK): Safety and Performance Division Winfrith Technology Centre; 1990. (AEEW-R 1863).

[20] Cissé S, Laffont L, Tanguy B, et al. Effect of surface preparation on the corrosion of austenitic stainless steel 304L in high temperature steam and simulated PWR primary water. Corros Sci. 2012;56:209–216.

[21] Bowsher B, Dickinson S, Nichols A. High temperature studies of simulant fission products: Part I, Vapour deposition and interaction of caesium iodide, caesium hydroxide, and

tellurium with stainless steel. Winfrith (UK): Atomic Energy Authority; 1983. (AEEW-R 1697).

[22] Sallach R, Elrick R, Douglas S, et al. Reaction between some cesium-iodine compounds and the reactor materials 304 stainless steel Inconel 600 and silver. Volume II. Cesium iodide reactions. Sandia National Labs., Albuquerque, NM (USA); 1986.

[23] Kobata M, Okane T, Nakajima K, et al. Chemical form analysis of reaction products in Cs-adsorption on stainless steel by means of HAXPES and SEM/EDX. J Nucl Mater. 2018;498:387–394.

[24] Baston VF, Hofstetter KJ, Bain GM, et al. A comparison of TMI-2 and laboratory results for cesium activity retained on reactor material-surfaces. In: Transactions of the American Nuclear Society; Vol. 50; American Nuclear Society; Illinois (IL); 1985. p. 223–225.

[25] Di Lemma F, Nakajima K, Yamashita S, et al. Surface analyses of cesium hydroxide chemisorbed onto type 304 stainless steel. Nucl Eng Des. 2016;305:411–420.

[26] Di Lemma F, Nakajima K, Yamashita S, et al. Experimental investigation of the influence of Mo contained in stainless steel on Cs chemisorption behavior. J Nucl Mater. 2017; 484:174–182.

[27] Nishioka S, Nakajima K, Suzuki E, et al. An experimental investigation of influencing chemical factors on Cs-chemisorption behavior onto stainless steel. J Nucl Sci Technol. 2019;56(11):988–995.

[28] Ngarayana IW, Murakami K, Do TMD. Effect of surface oxidation on the cesium chemisorption behavior of SS 304, Inconel 600 and X-750. J Nucl Sci Technol. 2022; 59(8):993–1003.

[29] Nakajima K, Nishioka S, Suzuki E, et al. Study on chemisorption model of cesium hydroxide onto stainless steel type 304. Mech Eng J. 2020;7(3). 19-00564.

[30] Osaka M, Gouëllo M, Nakajima K. Cesium Chemistry in the LWR severe accident and towards the decommissioning of Fukushima Daiichi Nuclear Power Station. J Nucl Sci Technol. 2022;59(3):292–305.

[31] Ngarayana IW, Murakami K, Suzuki T, et al. Role of solute titanium and oxidation in cesium chemisorption onto stainless steel. J Nucl Sci Technol. 2023;60(6):669–677.

[32] Technical Strategic Plan 2022 for Decommissioning of the Fukushima Daiichi Nuclear Power Station of Tokyo Electric Power Company Holdings, Inc. Tokyo (Japan): Nuclear Damage Compensation and Decommissioning Facilitation Corporation; 2022.

[33] Gauntt RO, Kalinich DA, Cardoni JN, et al. Fukushima Daiichi accident study: status as of April 2012. Albuquerque (NM) and Livermore (CA): Sandia National Laboratories; 2012. (SAND2012-6173).

[34] Bonneville H, Carénini L, Barrachin M, et al. Fukushima core melt composition simulation with ASTEC. In: 16th International Topical Meeting on Nuclear Reactor Thermalhydraulics (NURETH-16); 2015 Aug 30–Sept 4; Chicago, USA; Illinois (IL). American Nuclear Society; 2015. p. 4005–4018.

[35] Bull SJ. Failure mode maps in the thin film scratch adhesion test. Tribol Int. 1997; 30(7):491–498.

[36] Bull SJ, Berasetegui EG. An overview of the potential of quantitative coating adhesion measurement by scratch testing. Tribol Int. 2006;39(2):99–114.

[37] Steinmann PA, Hintermann HE. A review of the mechanical tests for assessment of thinfilm adhesion. J Vac Sci Technol A. 1989;7(3):2267–2272.

[38] Perry AJ. Scratch adhesion testing: a critique. Surf Eng. 1986;2(3):183–190.

[39] Perry AJ. The adhesion of chemically vapour-deposited hard coatings to steel—the scratch test. Thin Solid Films. 1981;78(1):77–94.

[40] Perry AJ, Valli J, Steinmann PA. Adhesion scratch testing: A round-robin experiment. Surf Coat Technol. 1988;36(1-2):559–575.

[41] Sekler J, Steinmann PA, Hintermann HE. The scratch test: Different critical load determination techniques. Surf Coat Technol. 1988;36(1-2):519–529.

[42] Pfoertsch et al ; 1983. ICDD No: 00-054-0331.

[43] Swanson HE, McMurdie HF, Morris MC, et al. Standard X-ray Diffraction Powder Pat-

terns. U. S. Department of Commerce National Bureau of Standards; 1967. NBS Monograph 25 - Section 5.

[44] Zheng L, Hosoi K, Ueda S, et al. Si-rich phases and their distributions in the oxide scale formed on 304 stainless steel at high temperatures. J Nucl Mater. 2018;507:327–338.

[45] Morris MC, McMurdie HF, Evans EH, et al. Standard X-ray Diffraction Powder Patterns Section 18 - Data for 58 Substances. U. S. Department of Commerce National Bureau of Standards & JCPDS - International Centre for Diffraction Data; 1981.

[46] McMurdie HF, Morris MC, Evans EH, et al. Standard X-ray diffraction powder patterns from the JCPDS research associateship. Powder Diffr. 1987;2(1):41–52.

[47] Song E, Suh D, Bhadeshia H. Oxidation of silicon containing steel. Ironmak Steelmak. 2012;39(8):599–604.

[48] Gates-Rector S, Blanton T. The Powder Diffraction File: a quality materials characterization database. Powder Diffr. 2019;34(4):352–360. ICDD No: 00-051-0115.

[49] Alekseeva ZD. The Cs_2O–SiO_2 system. Russ J Inorg Chem. 1966;11:626–629.

[50] Scheetz B, Pfoertsch D, Marks J ; 1994. ICDD No: 00-045-0418.

[51] Fjellvåg H, Grønvold F, Stølen S, et al. On the crystallographic and magnetic structures of nearly stoichiometric iron monoxide. J Solid State Chem. 1996;124(1):52–57.

Table 1. Compositions of the SS304 substrates.

Sample no.	Composition, wt%					
	Si	Cr	C	Ni	Fe	Others
1-6	0.20	19.37	0.032	8.97	70.5	1.26
8-12	1.02	19.48	0.035	8.97	70.0	1.29

Table 2. Sample chemisorption conditions.

No.	Substrate	Treatment	Si wt.%	Temperature K	Atmosphere
1	SS304	CsOH	0.2	1073	Ar/H_2
2	SS304	CsOH	0.2	1073	$Ar/H_2/H_2O$
3	SS304	CsOH	0.2	1273	Ar/H_2
5	SS304	CsOH	0.2	1273	$Ar/H_2/H_2O$
6	SS304	-	0.2	1273	$Ar/H_2/H_2O$
8	SS304	CsOH	1.0	1073	$Ar/H_2/H_2O$
9	SS304	CsOH	1.0	1273	Ar/H_2
11	SS304	CsOH	1.0	1273	$Ar/H_2/H_2O$
12	SS304	-	1.0	1273	$Ar/H_2/H_2O$

Table 3. Scratch test conditions.

Parameters	Value
Begin load	0.9 N
End load	70 N
Loading rate	100 N/min
Scratch speed	10 mm/min
Test repeating numbers	3 times per side
Temperature	297 - 299 K
Humidity	24 - 29%

Table 4. Cohesive failure modes and their corresponding dust generation levels.

Mode	Observed morphology	Dust generation
Crack (L_{c1})	Cracks on the scale's surface	Minor
Point 1 (L_{c2})	Isolated glossy patches (width > 20 μm)	Moderate
Point 2 (L_{c3})	Continuous glossy regions	Major

Table 5. Critical loads of each oxide scale's cohesive failure modes.

Sample no.	Sample information	L_{c1}, N	L_{c2}, N	L_{c3}, N
1	0.2 wt.% Si 1073K Ar/H_2	12.8±0.7	15.1±0.5	18.9±1.1
2	0.2 wt.% Si 1073K $Ar/H_2/H_2O$	15.7±0.5	18.1±1.3	22.0±1.9
3	0.2 wt.% Si 1273K Ar/H_2	16.0±0.9	18.9±0.8	22.4±0.4
5	0.2 wt.% Si 1273K $Ar/H_2/H_2O$	16.3±0.3	17.7±0.2	19.7±0.4
6	0.2 wt.% Si 1273K $Ar/H_2/H_2O$[a]	14.6±0.9	25.2±2.3	31.3±0.5
8	1.0 wt.% Si 1073K $Ar/H_2/H_2O$	18.4±0.6	30.0±2.4	37.0±2.6
9	1.0 wt.% Si 1273K Ar/H_2	15.6±0.8	21.4±1.1	30.6±2.0
11	1.0 wt.% Si 1273K $Ar/H_2/H_2O$	18.5±0.7	21.4±1.7	29.2±1.6
12	1.0 wt.% Si 1273K $Ar/H_2/H_2O$[a]	14.9±1.1	29.6±3.4	38.1±2.9

[a]Non-chemisorbed SS304 sample.
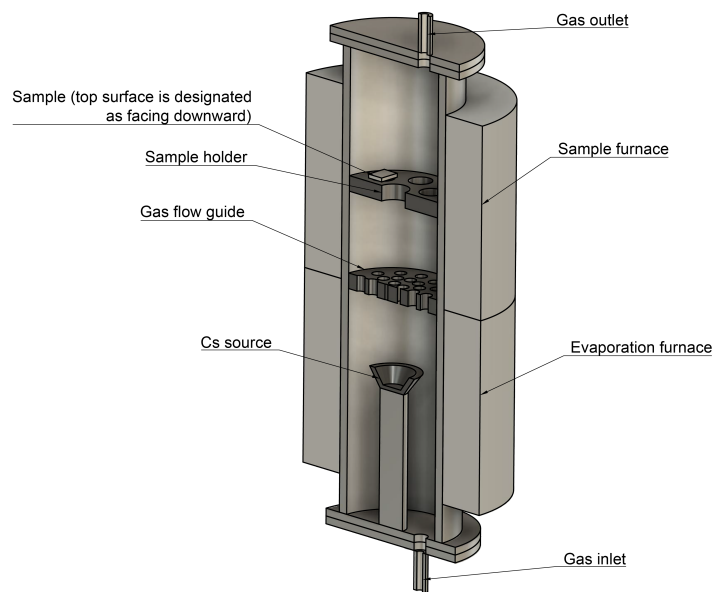
Figure 1. Simplified cross-sectional view of the CsOH chemisorption setup.
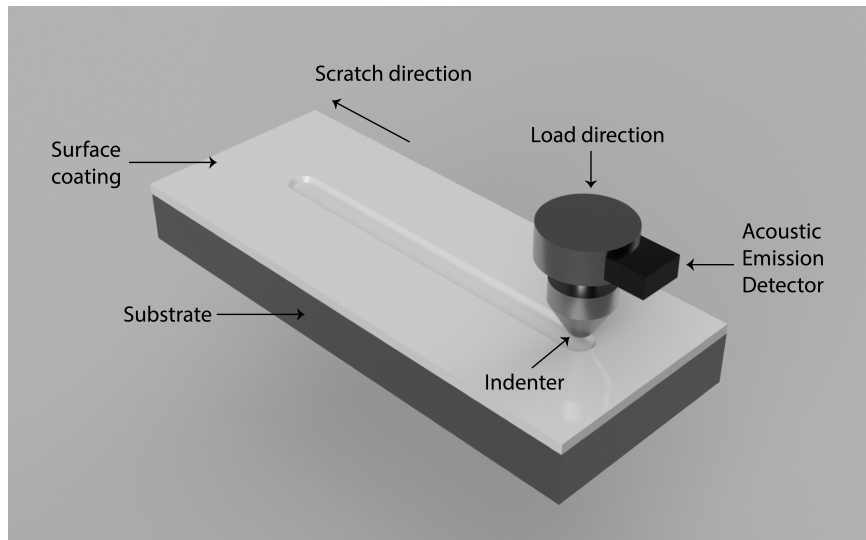
Figure 2. Simplified schematic of the Revetest Scratch Tester (RST).
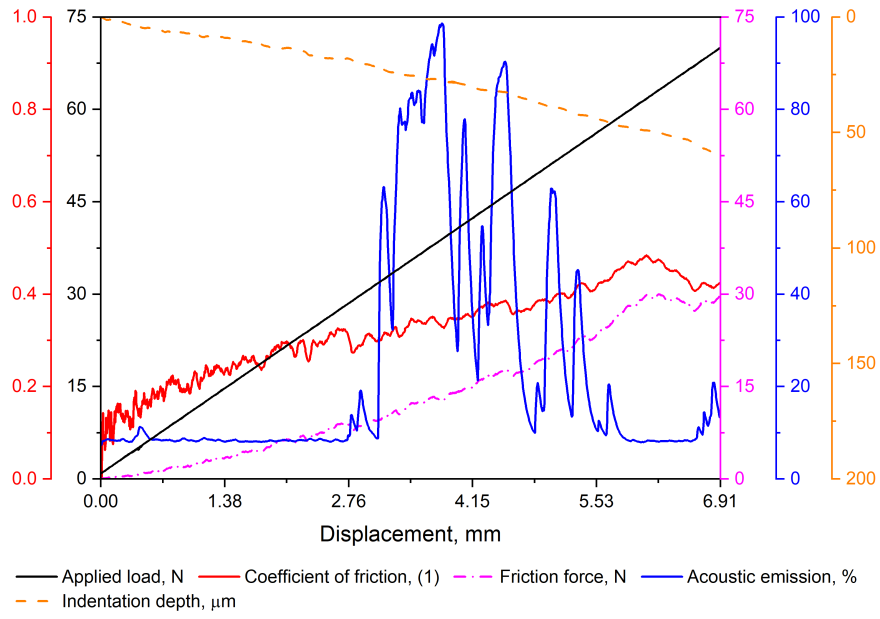
Figure 3. An example of the data recorded by the Revetest Scratch Tester.
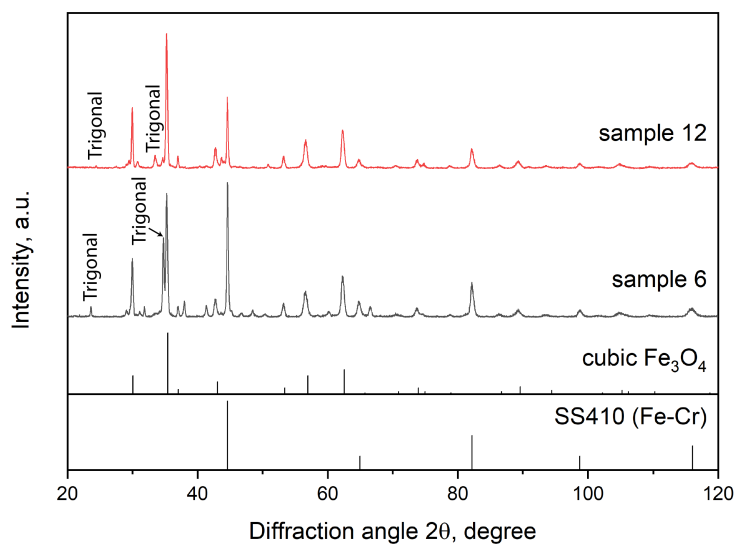
Figure 4. XRD patterns of non-chemisorbed samples 6 (0.2 wt.% Si, 1273 K, $Ar/H_2/H_2O$) and 12 (1.0 wt.% Si, 1273 K, $Ar/H_2/H_2O$).
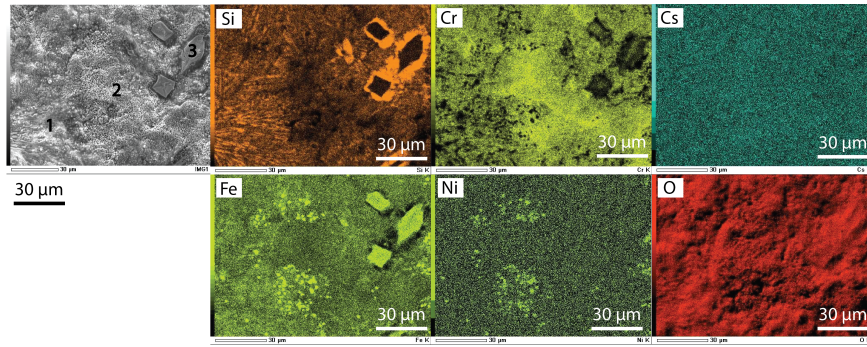
Figure 5. SEM–EDS surface analyses of non-chemisorbed sample 12 (1.0 wt.% Si, 1273 K, Ar/H$_2$/H$_2$O).
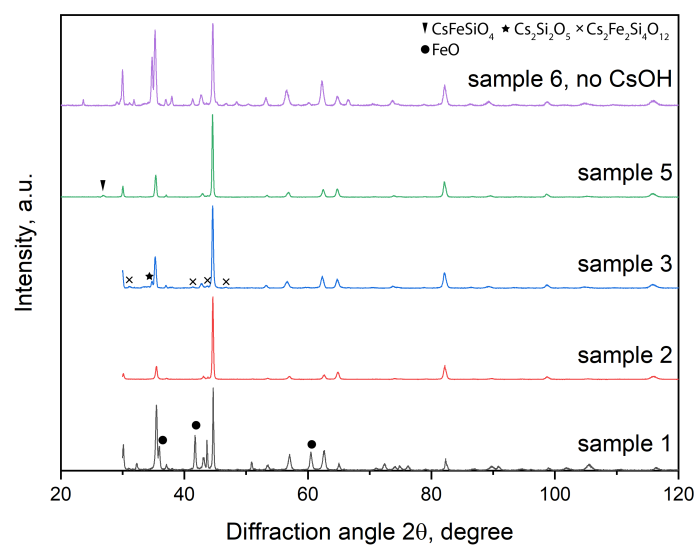
Figure 6. XRD patterns of CsOH-chemisorbed samples with 0.2 wt.% Si, compared to that of non-chemisorbed sample 6 (0.2 wt.% Si, 1273 K).
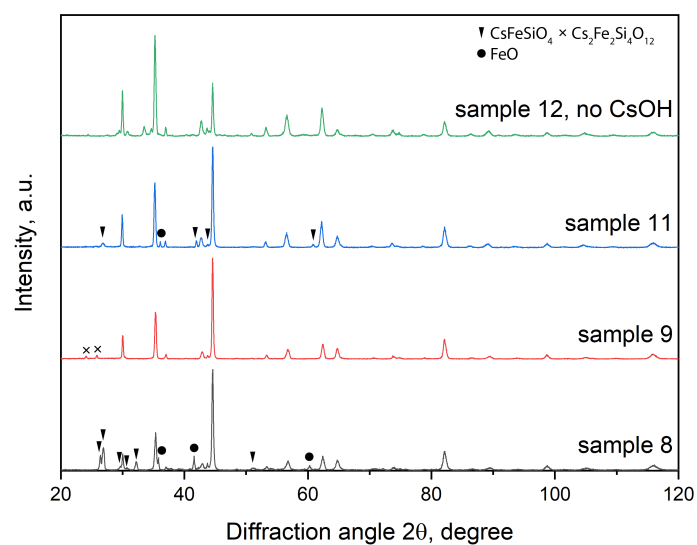
Figure 7. XRD patterns of CsOH-chemisorbed samples with 1.0 wt.% Si, compared to that of non-chemisorbed sample 12 (1.0 wt.% Si, 1273 K).
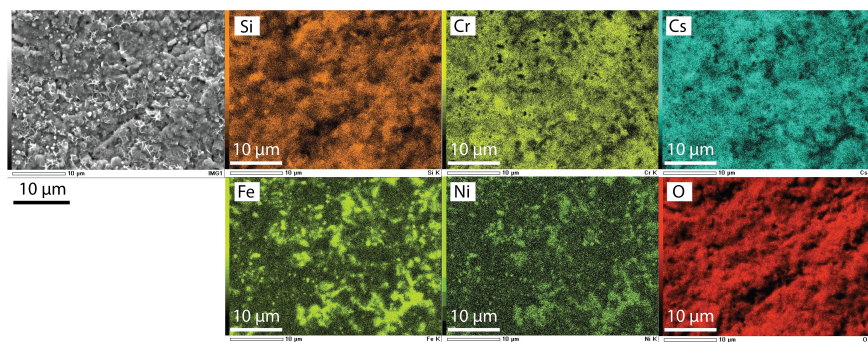
Figure 8. SEM–EDS surface analyses of CsOH-chemisorbed sample 8 (1.0 wt.% Si, 1073 K, $Ar/H_2/H_2O$).
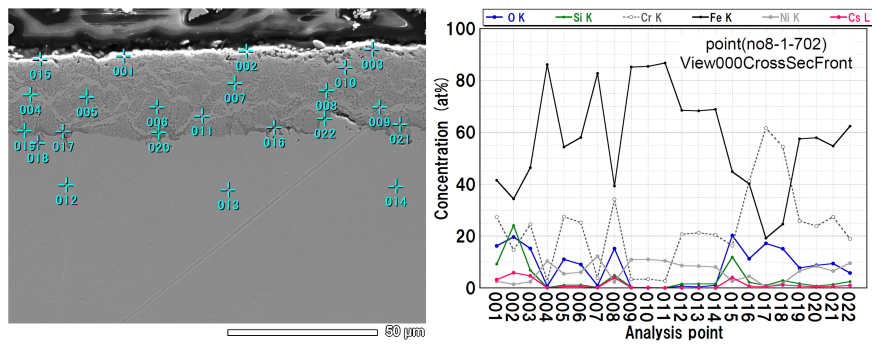
Figure 9. Cross-sectional SEM–EDS analysis of CsOH-chemisorbed sample 8 (1.0 wt.% Si, 1073 K, Ar/H$_2$/H$_2$O).
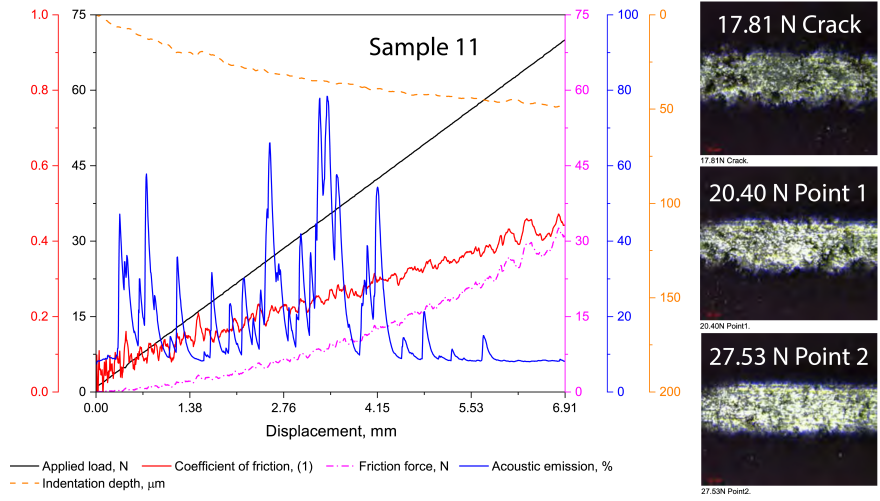
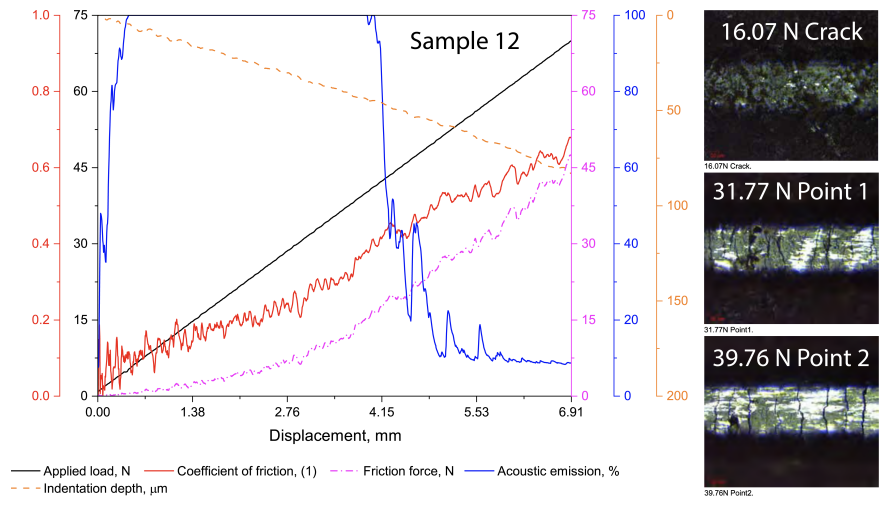**Figure 10.** Optical microscopic images and recorded data of CsOH-chemisorbed sample 11 (1.0 wt.% Si, 1273 K, Ar/H$_2$/H$_2$O).

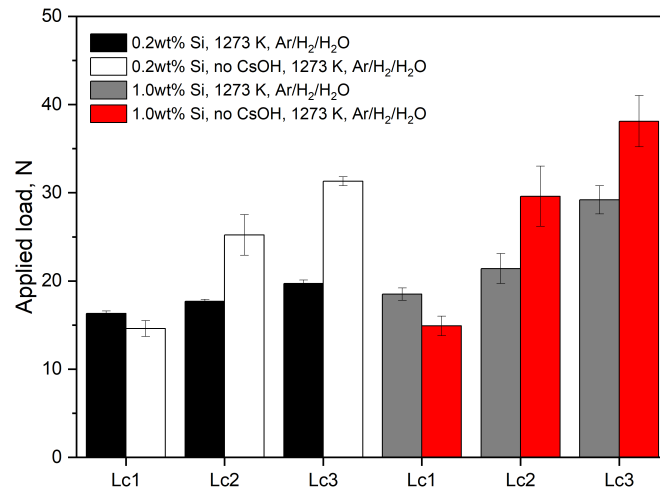**Figure 11.** Optical microscopic images and recorded data of non-chemisorbed sample 12 (1.0 wt.% Si, 1273 K, Ar/H_2/H_2O).

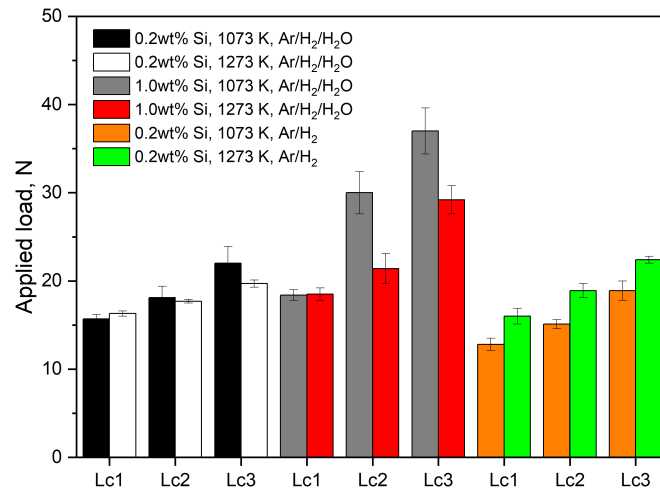**Figure 12.** Effect of CsOH-chemisorption on the critical loads.

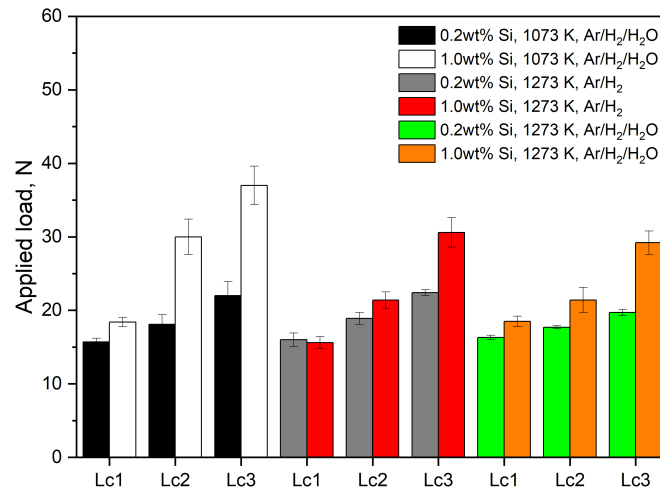**Figure 13.** Effect of temperature on the critical loads.

Figure 14. Effect of silicon concentration in SS304 on the critical loads.